Constrained Geometry Relaxations in Materials Science

Maja-Olivia Lenz,[1] Thomas A. R. Purcell*,[1] David Hicks,[2]
Stefano Curtarolo,[2] Matthias Scheffler,[1] and Christian Carbogno[1]

[1] *Fritz-Haber-Institut der Max-Planck-Gesellschaft, Faradayweg 4–6, D-14195 Berlin, Germany*
[2] *Department of Materials Science and Mechanical Engineering, Duke University, Durham, NC 27708, USA*

(Dated: August 6, 2019)

Reducing parameter spaces via exploiting symmetries has greatly accelerated and increased the quality of electronic-structure calculations. Unfortunately, many of the traditional methods fail when the global crystal symmetry is broken, even when the distortion is only a slight perturbation (e.g. Jahn-Teller like distortions). Here we introduce a flexible, user-defined parametric relaxation scheme, and implement it in the all-electron code FHI-aims. This approach utilizes geometeric constraints to maintain symmetry at any level. After demonstrating the method's ability to relax metastable structures, we highlight its adaptability and performance over a test set of 340 materials, across thirteen lattice prototypes. Finally we show how these constraints can reduce the number of steps needed to relax local lattice distortions by an order of magnitude. The flexibility of these constraints enables a significant acceleration of the high-throughput searches for novel materials and crystal structures.

I. INTRODUCTION

Symmetry preservation and breaking is one of the most fundamental processes in physics and chemistry. Many properties and applications such as, piezoelectricity [1–4], pyroelectricity [5, 6], ferroelectricity [7–10], topological insulators [11, 12], and non-linear optics [13–15], require certain selection rules to be met, and therefore require certain crystollagraphic symmetries to be maintained. Furthermore, it is not only **global** symmetry, the space and point groups of a material, but also **local** symmetry breaking that matters. For example, defects can cause significant changes in a material's mechanical [16, 17] and optical [18, 19] properties as well as in its electronic [20–22] and thermal transport [23–25] coefficients. Selectively preserving and breaking a material's symmetries is therefore paramount in computational material science, especially in *high-throughput* studies, which often aim to discover novel materials with improved properties by systematically scanning through material space. To streamline such calculations it is essential to keep both global and local symmetries under control. This allows for the efficient targeting of specific geometric configurations and avoids revisiting and recalculating already investigated configurations.

Traditionally, crystallographic symmetries are incorporated in first-principles codes already at the electronic-structure level (e.g., by sampling $\boldsymbol{k}$-space grids in the irreducible part of the Brillouin zone [26] or by sampling real space in symmetry defined "irreducible wedges" [27]) since it leads to significant savings in memory and computational workload for highly symmetric crystals. Also, by this means the obtained forces on the atoms and stresses on the lattice vectors fully reflect the crystallographic symmetries. Since geometry relaxation algorithms such as steepest descent, conjugate gradient, Newton-Raphson, quasi-Newton (e.g. BFGS [28]), and truncated-Newton methods [29] rely on the forces and stresses to update the atomic and lattice degrees of freedom, **global** symmetries are inherently preserved in such approaches. However, this does not allow for **local** symmetry breaking. To address such cases in first-principles calculations, it is typically necessary to lift all crystallographic symmetry constraints and treat the atomic and lattice degrees of freedom as a set of freely changing parameters. Besides the increased computational cost, such unconstrained structure optimization can lead to long and inefficient relaxation trajectories. While this issue can be alleviated by representing the structure via internal coordinates [30, 31], targeting a specific local symmetry typically requires manual inspection and analysis by the user. This is particularly cumbersome if multiple, competing structures with different local configurations need to be addressed.

Here we present a scheme to incorporate geometric constraints in structure optimizations that treats **global** and **local** symmetries equally. The proposed approach employs a mapping of the relevant degrees of freedom onto a lower-dimensional representation of the structure; the respective forces and stresses are then automatically mapped in this reduced representation. With that, the implemented formalism does not require to alter the employed relaxation algorithm, while still allowing the introduction of arbitrary constraints in a user-friendly manner. We first describe how the methodology works and the tools that can be used to quickly generate new structures. We demonstrate that these constraints allow to perform geometry optimizations for dynamically stabilized structures, which are not easily addressable otherwise. By analyzing the constrained and unconstrained relaxations of a test set of 340 materials, we then show that these constraints are also computationally beneficial for the relaxation of stable materials. Finally we illustrate how the parameters can be used to preserve **local symmetries** and accelerate relaxations in supercells.

II. METHODS

A. Transformation to reduced space

For a free relaxation, the optimizer acts on the full $3N+9$ dimensional potential-energy surface $E(\boldsymbol{R}, \boldsymbol{L})$ of a material, which is encoded by the atomic, $\boldsymbol{R}$, and lattice, $\boldsymbol{L}$, degrees of freedom. The lattice degrees of freedom are stored as the three components of the three lattice vectors in the chosen unit cell, and the atomic degrees of freedom are the $3N$ possible positions of the N atoms in a unit cell, represented by Cartesian or fractional coordinates. The forces, $\boldsymbol{F}$, acting on the atomic degrees of freedom are the derivatives the energy with respect to $\boldsymbol{R}$

$$\boldsymbol{F} = -\frac{dE}{d\boldsymbol{R}}, \tag{1}$$

while the forces acting on the lattice vectors stem from the stresses σ

$$\sigma = \frac{1}{V}\frac{dE}{d\boldsymbol{L}}, \tag{2}$$

where V is the volume of the unit cell. In *ab initio* approaches, E is determined by solving the electronic-structure problem, and the respective derivatives are obtained analytically via the Hellmann-Feynman Theorem. However, in practice this requires to account for additional terms, such as the Pulay terms and multipole corrections, as done in FHI-aims [32, 33].

Because the underlying potential-energy surfaces (PES) are complex, relaxing certain polymorphs of a material on these surfaces can be challenging or even impossible. As an example, zirconia (ZrO_2) can exist in its pure form in three different crystal phases: a high temperature ($T > 2370\,^{\circ}\mathrm{C}$) cubic phase, an intermediate temperature ($1170\,^{\circ}\mathrm{C} \leq T \leq 2370\,^{\circ}\mathrm{C}$) tetragonal phase, and a low temperature ($T < 1170\,^{\circ}\mathrm{C}$) monoclinic phase [34]. When transitioning from the cubic phase to the tetragonal phase the oxygen atoms distort along the c-axis of the tetragonal structure, and the lattice subsequently stretches along that direction [34]. To help illustrate this, in Figure 1a we plot a two dimensional PES for a twelve atom zirconia unitcell over a reduced parameter set taken from the AFLOW Library of Crystallographic Prototypes. The library sorts materials by their space group, stoichiometry, and occupied Wyckoff sites, as calculated with AFLOW-SYM [35], placing all materials that share those features into the same crystal prototype [36, 37]. A reduced parameter space can then be generated from a prototype definition, and used to describe that class of materials. For example the tetragonal phase of zirconia can be described by only three parameters: length of the lattice vectors in the $\boldsymbol{a}$ and $\boldsymbol{b}$ directions (a), the ratio of the lattice vectors ($\frac{c}{a}$), and the magnitude of the oxygen distortions (z_2). If only oxygen distortions z_2 along the z-axis are allowed, the PES in Figure 1a has two wells corresponding to the equivalent tetragonal structures, and a saddle point between them representing a high-symmetry configuration, i.e., the the high-temperature cubic phase for $c = a$. On this PES, a free relaxation of the cubic phase would result in the material relaxing towards one of the two wells; however, by constraining the relaxation to act only on a, the stable cubic phase can be obtained as shown in the outsets in Figure 1a. While the same effects could be achieved by relaxing the cubic zirconia structure in its primitive cell, the minimum volume unit cell of a structure, some materials such as bismuth dioxide [38, 39], have high-temperature polymorphs with the same number of sites as their stable structures.

To help demonstrate how the constraints are used in a calculation, we provide a sample FHI-aims geometry input file for the twelve atom zirconia unitcell in Figure 1b. In a free relaxation the geometry of zirconia would be optimized over all of the components of the lattice vectors and the atomic coordinates, effectively allowing any of the input parameters to change. While this will find the lowest energy structure, the fully relaxed geometry may no longer be in the same phase as it began in, as the optimizer can push it towards a lower energy portion of the PES. However, once the parameter space is mapped onto one defined by the symmetry of the structure, only geometeries within the initial space group can be explored. For the tetragonal phase ZrO_2, this means that the optimizer can now act only on a, $\frac{c}{a}$, and z_2. To simplify the inputs the value of $\frac{c}{a} * a$ is reduced to simply c in Figure 1b. In practice this reduction means that only the colored and boldfaced components of the atomic positions and lattice vectors can change, and they must obey the equations in the symmetry_lv and symmtry_frac portion of file. Under these constraints both the cell and positions are allowed to relax without breaking the symmetry of the initial structure. A further reduction to the cubic cell is possible by respectively fixing the z_2 and $\frac{c}{a}$ to zero and one, and allowing only the diagonal elements of the cell to change.

The previous input example illustrates the flexibility of these constraints is shown in the previous example, but knowledge of which reduced parameters to use and their relation to the full geometry, must be known before generating an input file. For crystals, these are determined by the spacegroup and the Wyckoff positions and can therefore be manually constructed. Because the Wyckoof sites and space groups are part of AFLOW's crystal prototype definition, an easy way to get access many of these is through their utilities [36, 37]. For all prototypes defined in the library, the automatized generation of input geometries for VASP [26], FHI-aims [32], Quantum Espresso [40], Abinit [41] and more codes is supported by AFLOW. As of version 3.1.204, the option `--add_equations` can be added to the AFLOW command to generate FHI-

a)

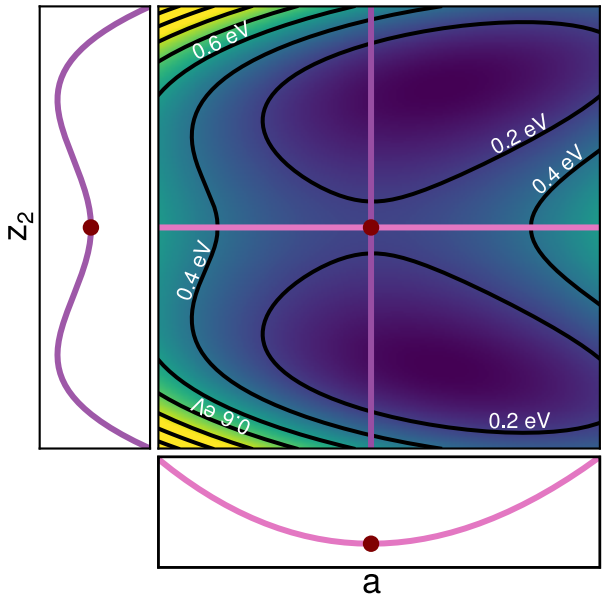

b)

```
lattice_vector 4.97 0.00 0.00
lattice_vector 0.00 4.97 0.00
lattice_vector 0.00 0.00 4.97

atom_frac 0.00 0.00 0.00 Zr
atom_frac 0.50 0.50 0.00 Zr
atom_frac 0.50 0.00 0.50 Zr
atom_frac 0.00 0.50 0.50 Zr
atom_frac 0.25 0.25 0.25 O
atom_frac 0.75 0.75 0.25 O
atom_frac 0.25 0.75 0.75 O
atom_frac 0.75 0.25 0.75 O
atom_frac 0.25 0.25 0.75 O
atom_frac 0.75 0.75 0.75 O
atom_frac 0.25 0.75 0.25 O
atom_frac 0.75 0.25 0.25 O

symmetry_n_params 3 2 1
symmetry_params a c z2
symmetry_lv a , 0 , 0
symmetry_lv 0 , a , 0
symmetry_lv 0 , 0 , c # c = (c/a)*a
symmetry_frac 0.00 , 0.00 , 0.00
symmetry_frac 0.50 , 0.50 , 0.00
symmetry_frac 0.50 , 0.00 , 0.50
symmetry_frac 0.00 , 0.50 , 0.50
symmetry_frac 0.25 , 0.25 , 0.25-z2
symmetry_frac 0.75 , 0.75 , 0.25-z2
symmetry_frac 0.25 , 0.75 , 0.75+z2
symmetry_frac 0.75 , 0.25 , 0.75+z2
symmetry_frac 0.25 , 0.25 , 0.75-z2
symmetry_frac 0.75 , 0.75 , 0.75-z2
symmetry_frac 0.25 , 0.75 , 0.25+z2
symmetry_frac 0.75 , 0.25 , 0.25+z2
```

FIG. 1. An illustration of the new relaxation scheme. a) A two- dimensional potential-energy surface for ZrO_2. The minimum energy structure is set to 0.0 eV and the contour lines correspond to a 0.2 eV increase in energy. The red dot represents a structure corresponding to a high temperature cubic phase of the material. The outsets show the one-dimensional potential-energy surface along each mode. b) The sample geometry input file for the tetragonal ZrO_2 in FHI-aims. The input geometry values are color coded to the reduced parameter that controls its value. For the cubic structures all non-itallics values are fixed.

aims `geometry.in` files already containing the additional block required for the constrained relaxation. Because of this, we use the crystal prototypes defined by the AFLOW Library of Crystallographic Prototypes throughout this work.

To accomplish the parameter space reduction in real materials, let us assume a (3×3)-dimensional lattice vector matrix $\boldsymbol{\mathcal{L}}$ and a $(N \times 3)$-dimensional matrix $\boldsymbol{\mathcal{R}_\mathcal{F}}$ for the fractional atomic positions. Given the atomic forces $\boldsymbol{\mathcal{F}_\mathcal{R}}$ on the fractional atomic positions and the stress tensor σ, we can calculate the derivatives of the energy with respect to the lattice components [42]

$$\frac{\mathrm{dE}}{\mathrm{d}\boldsymbol{\mathcal{L}}} = \boldsymbol{\mathcal{L}}^{T^{-1}} V \cdot \sigma \tag{3}$$

where V is the unit cell volume and obtain the generalized forces on the lattice $\boldsymbol{\mathcal{F}_\mathcal{L}}$ after cleaning from the atomic contributions

$$\boldsymbol{\mathcal{F}_\mathcal{L}} = -\frac{\mathrm{dE}}{\mathrm{d}\boldsymbol{\mathcal{L}}} - \boldsymbol{\mathcal{R}_\mathcal{F}}^T \boldsymbol{\mathcal{F}_\mathcal{R}}. \tag{4}$$

Each of these matrices denoted by calligraphic letters, $\boldsymbol{\mathcal{R}_\mathcal{F}}$, $\boldsymbol{\mathcal{F}_\mathcal{R}}$, $\boldsymbol{\mathcal{L}}$ and $\boldsymbol{\mathcal{F}_\mathcal{L}}$, can be flattened to one-dimensional vectors that we will name $\boldsymbol{R_F}$, $\boldsymbol{F_R}$, $\boldsymbol{L}$ and $\boldsymbol{F_L}$ respectively. In the parameter representation these quantities reduce to their small-letter counterparts, the M_R-dimensional $\boldsymbol{r}$, $\boldsymbol{F_r}$ and M_L-dimensional $\boldsymbol{l}$ and $\boldsymbol{F_l}$, via

$$\boldsymbol{r} = \boldsymbol{\mathcal{J}}_{\boldsymbol{Rf}}^{-1} \left(\boldsymbol{R_F} - \boldsymbol{t_{Rf}}\right) \tag{5a}$$

$$\boldsymbol{l} = \boldsymbol{\mathcal{J}}_{\boldsymbol{L}}^{-1} \left(\boldsymbol{L} - \boldsymbol{t_L}\right) \tag{5b}$$

$$\boldsymbol{F_r} = \boldsymbol{\mathcal{J}}_{\boldsymbol{Rf}}^{T} \boldsymbol{F_R} \tag{5c}$$

$$\boldsymbol{F_l} = \boldsymbol{\mathcal{J}}_{\boldsymbol{L}}^{T} \boldsymbol{F_L}. \tag{5d}$$

where $\boldsymbol{\mathcal{J}_{Rf}}$ and $\boldsymbol{\mathcal{J}_L}$ are the Jacobian matrix for the transformations and $\boldsymbol{t_{Rf}}$ and $\boldsymbol{t_L}$ are the transforma-

tion vectors for the respective fractional atomic and lattice degrees of freedom. The transformation vectors are used to include any constant shifts, which are not captured by the Jacobians. Because $\boldsymbol{\mathcal{J}_{Rf}}$ and $\boldsymbol{\mathcal{J}_{\mathcal{L}}}$ are not square and therefore not regularly invertible, we use the generalized left inverse [43] defined for a matrix $\boldsymbol{\mathcal{A}}$ as

$$\boldsymbol{\mathcal{A}}^{-1,L} = \left(\boldsymbol{\mathcal{A}}^T\boldsymbol{\mathcal{A}}\right)^{-1}\boldsymbol{\mathcal{A}}^T, \tag{6}$$

provided $\boldsymbol{\mathcal{A}}$ has full column rank. The transformation back to real space can then be performed by inverting Equations 5a-5d. The back-transformation of the forces to the full space is not necessary but can be helpful to obtain symmetrized Cartesian or Fractional forces, to check for the convergence of the relaxation.

To facilitate the construction of the Jacobian matrices, we assume a linear relationship between the full coordinates and the parameters. In principle, $\boldsymbol{\mathcal{J}_{Rf}}$ and $\boldsymbol{\mathcal{J}_{L}}$ can be constructed at each step by using analytical expressions to describe each real space degree of freedom as a function of the reduce parameter set; however, by assuming a linear relationship between the spaces they can be initialized at the start of the calculation and used at every step. For the atomic positions, this assumption is already fulfilled by using fractional instead of Cartesian coordinates. If we allow angles as unit cell parameters, which is the case for the monoclinic and triclinic lattice systems, the relations become non-linear containing for example expressions like $c \cdot \cos(\beta)$. In these cases the easiest solution is to substitute each non-zero lattice vector component with an independent parameter.

Before the relaxation the Hessian, $\boldsymbol{\mathcal{H}}$, is initialized in the full coordinate space, split into atomic and lattice blocks ($\boldsymbol{\mathcal{H}_R}$ and $\boldsymbol{\mathcal{H}_L}$ respectively), and individually transformed into reduced coordinate space, $\boldsymbol{\mathcal{H}_r}$ and $\boldsymbol{\mathcal{H}_l}$ via separate Jacobians, $\boldsymbol{\mathcal{J}_R}$ and $\boldsymbol{\mathcal{J}_L}$

$$\boldsymbol{\mathcal{H}_r} = \boldsymbol{\mathcal{J}_R}^T\boldsymbol{\mathcal{H}_R}\boldsymbol{\mathcal{J}_R} \tag{7}$$

$$\boldsymbol{\mathcal{H}_l} = \boldsymbol{\mathcal{J}_L}^T\boldsymbol{\mathcal{H}_L}\boldsymbol{\mathcal{J}_L}. \tag{8}$$

Here $\boldsymbol{\mathcal{J}_R}$ represents the transformation of the atomic coordinates from Cartesian space to the reduced space, which is calculated from $\boldsymbol{\mathcal{J}_{Rf}}$ by

$$\boldsymbol{\mathcal{J}_R} = \begin{pmatrix} \boldsymbol{\mathcal{L}} & 0 & \dots & 0 \\ 0 & \boldsymbol{\mathcal{L}} & \dots & 0 \\ \vdots & \vdots & \ddots & \vdots \\ 0 & 0 & \dots & \boldsymbol{\mathcal{L}} \end{pmatrix} \boldsymbol{\mathcal{J}_{Rf}}. \tag{9}$$

$\boldsymbol{\mathcal{J}_R}$ is then divided by the average unit vector length, $V^{1/3}$, so $\boldsymbol{\mathcal{H}_r}$ and $\boldsymbol{\mathcal{H}_l}$ are on a similar scale. The total Hessian is then recombined resulting in

$$\boldsymbol{\mathcal{H}} = \begin{pmatrix} \boldsymbol{\mathcal{H}_r} & 0 \\ 0 & \boldsymbol{\mathcal{H}_l} \end{pmatrix}. \tag{10}$$

Figure 2 illustrates the procedure for relaxing structures with these constraints. During the relaxation, a full SCF cycle is completed to obtain the forces and the stress tensor for the current geometry, at each step. If the convergence criterion is fulfilled, i.e. if the forces are below a given threshold, then the relaxation stops and returns the current geometry. Otherwise the lattice vectors as well as the atomic positions and their respective forces are mapped onto the reduced space using the transformation described in Equations 5a-5d. The atomic coordinates and forces are respectively scaled by $V^{1/3}$ and $V^{-1/3}$, and then passed on to the optimizer. In FHI-aims this is usually a BFGS/TRM optimizer. Once the optimized parameters are obtained, the full geometry is reconstructed from the parameters and a new relaxation step can begin.

B. Data Availability

The full input and output files for the calculations in this work are available in the NOMAD repository with the identifier [DOI: 10.17172/NOMAD/2019.08.05-1] [44].

III. APPLICATIONS AND BENCHMARKS

A. Relaxing Metastable and Unstable Systems

In some cases, constraining a relaxation is necessary to keep the structure in its given polymorph. Similar to what was seen for zirconia, a material can have many phases that metastable or unstable at zero point conditions that are stabilized by entropic contributions at higher temperatures or pressures. Here we define a metastable phase to be one that is in a local minimum on its PES. While freely relaxing stable or metastable structures is possible by respectively using an initial geometry near its correponding global or local minimum on the PES, unstable systems will tend to relax towards lower energy and usually lower-symmetric structures, unless they are somehow constrained. To demonstrate the ability of these constraints to optimize such structures, we relax the twelve atom cubic zirconia unitcell from Figure 1. While most relaxations will be performed on the primitive cells of structures, we use this system as a simple, demonstrative example. All calculations are done using the FHI-aims package, a full-potential, all-electron electronic structure code. FHI-aims utilizes numeric atom-centered orbital basis functions, grouped into different tiers beyond the minimal set needed to describe free atoms. For these calculations we use *tier 1* (double numeric plus polarization basis set) with *light* basis settings which were shown to calculate the lattice parameter and cohesive energy of face-centered cubic gold within 0.001 Å and 20 meV [32], respectively. We use

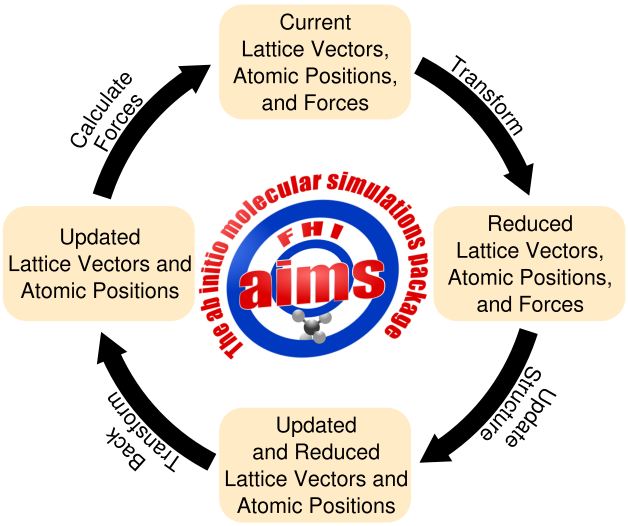

FIG. 2. Workflow of the relaxation constrained to the "parameter reduced space".

the PBEsol as the exchange-correlation functional; SCF convergence criteria of 10^{-6} eV/Å and 5×10^{-4} eV/Å for the density and forces, respectively; and the structures are relaxed until the maximum forces on the degrees for freedom are below 0.005 eV/Å. All other inputs were taken to be the default values in FHI-aims. While a larger basis set and using a hybrid functional would increase the accuracy of the calculations, we do not expect it to affect the performance of the relaxation scheme.

Figure 3a shows that using the constraints both the cubic and tetragonal phase of ZrO_2 can be converged in 4 and 10 steps, respectively, while only the tetragonal phase can be obtained in 30 steps with a free relaxation. The free relaxation of the cubic phase proceeds towards the tetragonal phase, but initially stalls at a non-physical simple cubic phase in 37 steps. If the relaxation convergence criteria is further reduced to 0.001 eV/Å the structure reaches the tetragonal phase in 114 steps.

Another example of a material with many metastable phases is bismuth oxide. Bismuth oxide exists in several different polymorphs [38] including the low temperature monoclinic phase α-; the high-temperature, face-centered cubic phase δ-; and the metastable, tetragonal phase β-Bi_2O_3 [39]. Upon heating α-Bi_2O_3 transforms into δ-Bi_2O_3 at around 730°C, and remains stable until it melts at approximately 825°C [39]. Depending on the cooling procedure, δ-Bi_2O_3 transitions to the β-phase or another metastable phase at approximtely 650°C [39]. Upon further cooling β-Bi_2O_3 returns to the α-Bi_2O_3 at ∼300°C [39]. Importantly, unlike ZrO_2, both the tetragonal and monoclinic phases have twenty atoms in their primitive cells, so both structures should be accessible from the other one. For these calculations we use the same computational settings as those used for ZrO_2, but with the *intermediate* settings for the basis set. The *intermediate* settings and basis sets in FHI-aims increases the accuracy of the default numerical settings, but more importantly adds an f-orbital to the double numeric plus polarization basis set for oxygen, which is necessary for describing monoclinic structures containing oxygen.

Figure 3b shows the relaxation for the tetragonal and monoclinic bismuth oxide phases. In both cases the constrained relaxation takes less time to converge with the constrained β- and α-phase needing 17 and 20 steps to converge, respectively. While for the α-phase removing the constraints simply increases the number of steps needed to converge system to 25 steps, the β-phase relaxes towards the α-phase, but stops an unknown, lower symmetry phase in 78 steps. Beyond the lower energy the final structure is both the lattice vectors and atomic coordinates are significantly different from both the starting and final constrained geometry meaning Since the free relaxation of the β-phase departs from the known phases of the material, a more in-depth study of it would be impossible without the constraints as the fully relaxed structures no longer represent the same material.

Both of these cases demonstrate the need for constraining relaxations to their crystal prototype for high-throughput applications. For the high-symmetry phases of both zirconia and bismuth oxide, the free relaxation not only initially converged to a different phase, but also unknown and potentially physically unrealizable ones. While the relaxation of ZrO_2 does eventually reach one of its known phases, bismuth oxide remains in incorrect structure. Any further calculations on those structures would be erroneous and could lead to both false positives and skewed property descriptors. While integrity checks could be made for some of the materials, the consistent breaking of they system's symmetry and the in-

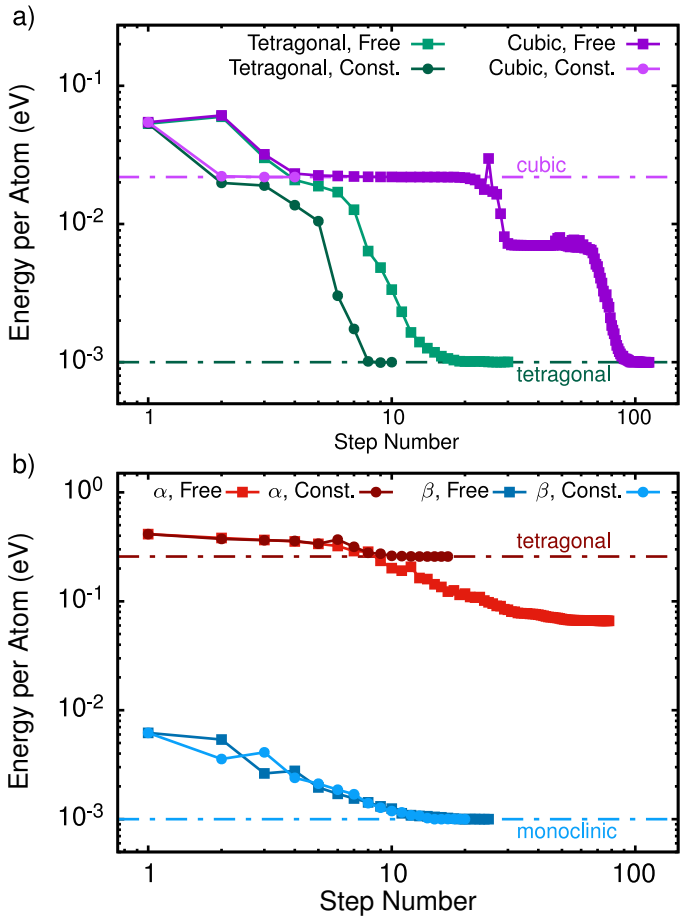

FIG. 3. Convergence behaviour of the free (squares) and constrained (circles) relaxations for a) the tetragonal phase (green) and cubic (purple) phases of ZrO_2 and b) the tetragonal (red) and monoclinic (blue) phase of Bi_2O_3. Both cubic phase of ZrO_2 and the tetragonal phase of Bi_2O_3 the free relaxation breaks the symmetry and finds an energetically lower structure which is the tetragonal phase for ZrO_2 and an unknown phase for Bi_2O_3. The energy scale on the y-axis is set to 1 meV below the minimum energy for each material.

consistent degree of that symmetry breaking makes developing standardized checks impractical. This will be particularly useful for crystal structure discovery where exact knowledge of lattice type and decorations is necessary.

B. Bench-marking the Algorithm

As the above examples show, the implemented constraints not only ensure that symmetry is preserved, but also accelerate the relaxation because the optimization of a reduced representation with less free parameters space is by definition a less demanding task. To quantify this, the new relaxation algorithm is tested on a set of 340 materials across multiple lattice systems and AFLOW prototypes, as summarized in Table I. The initial geometry of each material is taken from either the AFLOW [45] or Materials Project [46] database and converted into the right format using the Atomic Simulation Environment [47]. All relaxations are done in FHI-aims using the same settings as the zirconia calculations, using both the PBE and PBEsol functionals.

Table II and Figure 4 illustrates the largest benefit of using the constraints: the preservation of the initial crystallographic prototypes. Approximately 7% of all materials tested relax to a different structure according to the AFLOW-XTAL-MATCH tool [48]. This tool measures the similarity between two materials using techniques similar to those of Burzlaff, et al.[49] and produces a misfit value, m,

$$m = 1 - (1 - \text{dev})(1 - \text{disp})(1 - \text{fail}), \qquad (11)$$

where dev, disp, and fail are normalized representations of deviations in the lattice vectors, atomic positions, and a failure indicator for when an atomic deviation is more than half the shortest distance in the coordination polyhedra. From m we can determine if a structure is considered a match using the following mapping

$$\begin{aligned} m &\leq 0.1 : \text{structure are similar} \\ 0.1 < m &\leq 0.2 : \text{structures are within same family} \\ m &> 0.2 : \text{structures are not compatible.} \end{aligned}$$

TABLE I. Summary of the materials used in the test dataset

AFLOW Prototype	Space Group	# of Materials	Atoms per Unitcell	Free Parameters	Full d.o.f. / # Free Parameters
AB_oP8_62_c_c	62	8	8	7	4.71
A2B_oP12_62_2c_c	62	35	12	9	5.00
A2BC4_tI14_82_bc_a_g	82	35	7	5	6.00
A2BC4D_tI16_121_d_a_i_b	121	29	8	4	8.25
AB2_hP3_164_a_d	164	25	3	3	6.00
AB_hP4_186_b_b	186	37	4	2	5.25
AB_cF8_216_c_a	216	35	2	1	15.00
ABC_cF12_216_b_c_a	216	42	3	1	18.00
AB2C_cF16_225_a_c_b	225	11	4	1	21.00
AB2_cF12_225_a_c	225	13	3	1	18.00
AB_cF8_225_a_b	225	17	2	1	15.00
A_cF8_227_a	227	3	2	1	15.00
A2BC4_cF56_227_d_a_e	227	50	14	2	25.50

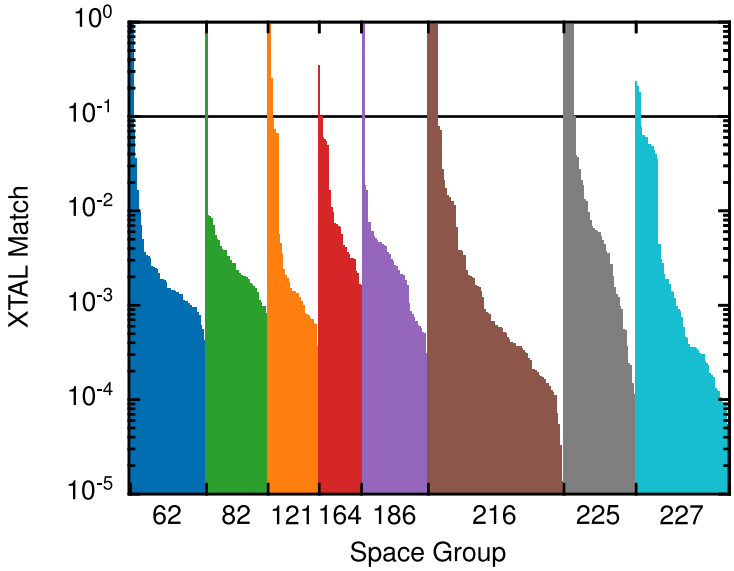

FIG. 4. The misfit between the fully and constrained relaxed structures using AFLOW-XTAL-MATCH. All structures below the horizontal line are considered matching. The structures are ordered by spacegroup and then by m

All the 22 materials with divergent relaxations in the data set follow the same pattern as ZrO_2 and Bi_2O_3. Therefore constraining these material's relaxation is vital because without them all further calculations on these materials would no longer be physically relevant.

Constraining the relaxation has benefits even when the final structures are similar as it significantly reduces the number of steps needed for the trajectories to converge. When the constrained and free relaxations proceed towards the same structures, the constraints reduce the number of relaxation steps by an average of 32.51% and 49.74% for calculations using the PBE and PBEsol functional, respectively. Including the divergent structures respectively decreases the saving to 31.75% and 49.01%, but this is expected as the constrained relaxation and free relaxations are acting on qualitatively different PESs. Here we define the savings, S, as

$$S = \frac{N_{\text{free}} - N_{\text{constrained}}}{N_{\text{constrained}}} \times 100\% \qquad (12)$$

where N_{free} is the number of steps need to converge the free relaxation and $N_{\text{constrained}}$ is the number of steps need to converge the constrained relaxation. The seemingly better performance of the constraints when using the PBEsol, is likely because of larger differences between the initial and final structures when using this functional. On average comparing the starting geometries with the freely relaxed ones gave an average m of 0.09451 (0.02926 when $m \neq 1$) and 0.1418 (0.03223 when $m \neq 1$) for the PBE and PBEsol calculations, respectively. And since increasing the distance to the final structure

TABLE II. Summary of the free and constrained relaxation performance by AFLOW prototype.

AFLOW Prototype	Space Group	# of Materials	PBE Average Savings	PBE # Preserved Space Group Free	PBE # XTAL Match	PBEsol Average Savings	PBEsol # Preserved Space Group Free	PBEsol # XTAL Match
AB_oP8_62_c_c	62	8	10.23	3	8	24.61	4	8
A2B_oP12_62_2c_c	62	35	10.84	19	29	18.32	20	33
A2BC4_tI14_82_bc_a_g	82	35	23.25	29	32	51.75	28	34
A2BC4D_tI16_121_d_a_i_b	121	29	35.44	23	26	47.69	21	26
AB2_hP3_164_a_d	164	25	7.03	10	24	19.68	5	24
AB_hP4_186_b_b	186	37	30.34	23	36	41.68	19	36
AB_cF8_216_c_a	216	35	31.41	26	34	54.47	29	34
ABC_cF12_216_b_c_a	216	42	42.88	32	42	72.91	30	37
AB2C_cF16_225_a_c_b	225	11	25.16	9	11	79.47	5	9
AB2_cF12_225_a_c	225	13	57.63	8	9	54.20	7	9
AB_cF8_225_a_b	225	17	36.32	9	17	51.19	6	17
A_cF8_227_a	227	3	35.12	3	3	47.62	3	3
A2BC4_cF56_227_d_a_e	227	50	67.10	37	47	73.58	37	47
Full Dataset		340	31.75	67.94%	93.52%	49.01	62.94%	93.24%

also increases the likelihood of the free relaxation deviating from the constrained trajectory, larger savings using the PBEsol functional is expected. This is also supported by the larger differences between the final structures of constrained and free relaxations for the PBEsol functional.

Unfortunately, the savings are not consistent across the various prototypes. Figure 5 shows the total number of steps needed to relax the structures with and without constraints for the PBEsol calculations, sorted by the space group and then the maximum number of relaxation steps needed. Similar to the average savings shown in Table II as the number of free parameters approaches the number of degrees of freedom in a material the savings from constraining the relaxation decrease. In some cases using the constraints actually increase the number of steps needed for the relaxation to converge, but in all of these cases the relaxation trajectories takes unproductive steps shown in the inset of Figure 5 for PtS_2. In these cases the extra free parameters allow the relaxation trajectories to pass the problematic regions faster and therefore converge to the final structures in fewer steps. These results suggest that for lower symmetry structures, the potential savings from constraining the relaxation can be considerably smaller.

Constraining the relaxation can also decrease the computational time needed to perform further calculations after the relaxations. Despite their similarity to the final geometries of the constrained relaxation, freely relaxed structures always break symmetry to some degree. To measure how well the relaxation preserves symmetry we compare the spglib calculated space groups of the initial and converged structures [50]. spglib calculates the space group of a material by iteratively searching for a given structure's primitive cell and symmetry operations and using those to generate the space group. The algorithm determines if a structure's space group has a certain symmetry operation, by checking if the operator transforms all the atoms in the structure to sites occupied by the same type of atom within a given small euclidean distance, ε. By default ε is set to 10^{-5} Å, and none of the tested materials remain in their initial space groups using this setting. To preserve the symmetry for the freely relaxed structures, a larger user-defined tolerance threshold is needed (0.01 Å is used in Table II), consistent with findings reported by Hicks, *et al.* [35]. However, when using the constraints, the symmetry is always perfectly preserved for all materials. This is advantageous as exploiting symmetry can greatly reduce the time needed to do further calculations for many applications. In particular phonon calculations using the finite difference approach where the symmetry of the system determines the number of atomic displacements, and therefore the number of force calculations, needed to calculate a complete set of force constants. By default Phonopy, a very popular Python package for calculating phonon spectra with finite differences [51], uses the default spglib settings to calculate the symmetry of a material, which would misrepresent all of the tested materials using free relaxation. Commensurate phonon calculations can be achieved by performing symmetry constrained relaxations and using more robust symmetry tools, such as AFLOW-SYM [35].

C. Systems with local symmetries or distortions

One of the key advantages of defining constraints in this way is the ability to locally break symmetry to account for point defects. While the previously

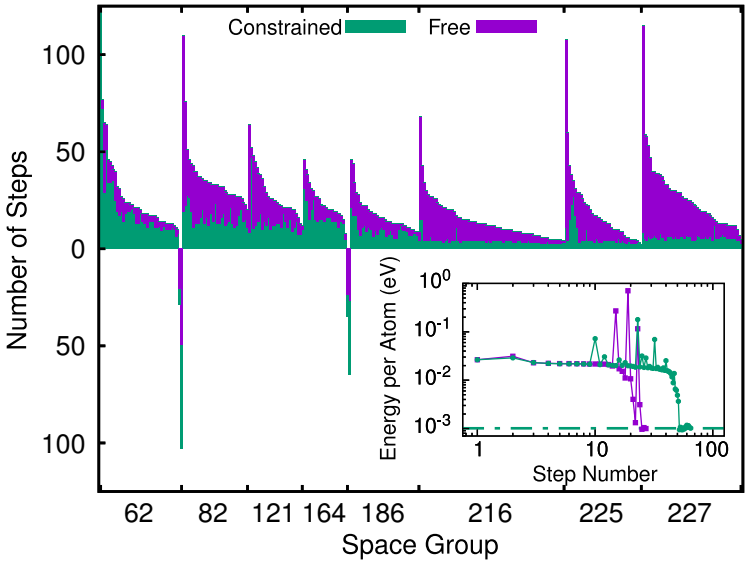

FIG. 5. The total number of steps needed for the constrained (green) and free (purple) relaxations. Negative step numbers represent the cases where the constrained relaxations take longer than the free relaxation. The bar for orthorhombic N_2O is not shown in the figure, the free relaxation took 310 steps, and the constrained one required 296 steps to converge. The inset shows the constrained (green circles) and free relaxation (purple squares) trajectory of platinum (IV) sulfide, which is one of the materials where the constrained relaxation takes more steps than the free relaxation. The zero of the energy scale is set to 1 meV below the energy of the relaxed structure (horizontal dashed line).

discussed benefits of lower relaxation times and relaxing unstable structures could also be achieved by using symmeterized forces, that method would not be able to locally break its symmetry. However many of these defects exhibit some type of short range order, such as Jahn-Teller-type lattice distortions [52–54], that can be parameterically added on top of the standard crystal structure. By including these distortions one can reduce the computational cost of relaxing supercells with defects, which is important when using a super cell approach to study point defects. This approach uses density functional methods to calculate the total energy of a system in a series of supercells of increasing size to study the effects of a defect on the system. If a scaling law is known for the system the results of these calculation can be extrapolated to the experimentally relevant dilute limit. As the supercell size increases the time needed to calculate each step also increases, therefore any reduction in the number of steps needed can save a significant amount of computational time.

To illustrate the ability of the new relaxation scheme to study point defects in materials, we study a polaronic distortion in MgO previously studied in our department [55]. Polarons are quasiparticles that couple point charges with lattice distortions in a material, reducing its charge carrier mobility. For rock salt MgO the lattice distortions for an electron hole polaron are Jahn-Teller like, and we generate a set of parameters to describe them for a 64 and 216 atom supercell. Figure 6 illustrates the uncorrected polaron energy for the free and constrained relaxation trajectories for these supercells [55]. Because charge localization is necessary when studying polarons, the HSE 2006 functional is used with a screening parameter of 0.11 Bohr^{-1} with exact exchange. The unrestricted spin relaxation converged the SCF density, forces, total energy, and eigenvalues were all converged to 10^{-4} eV/Å, 10^{-4} eV/Å, 10^{-5} eV, and 10^{-2} eV, respectively. Each atom calculated 5 empty states above those used by the Kohn-Sham orbitals and the structures were relaxed until the total forces on the free parameters were below 10^{-4} eV/Å. Starting from a distorted geometry the constrained relaxations take a fewer number of steps to converge the 64 and 216 atom supercells respectively needing 11 and 10 steps compared with 88 and 234 steps for the free relaxation. Using the constraints does cause the relaxation to converge to a structure with slightly higher energy, but this is because the chosen constraints are valid for an isolated polaron and thus do not account for the artificial interactions with periodic images due to the finite supercell size. In practice, this effect is rather negligible, since we find that the obtained polaron energy is 78.4 meV higher in energy than the free relaxation in the 2x2x2 supercell and 69.1 meV higher in the 3x3x3 supercell.

IV. CONCLUSIONS

In this work we presented a new scheme for parametrically relaxing structures in a user-defined,

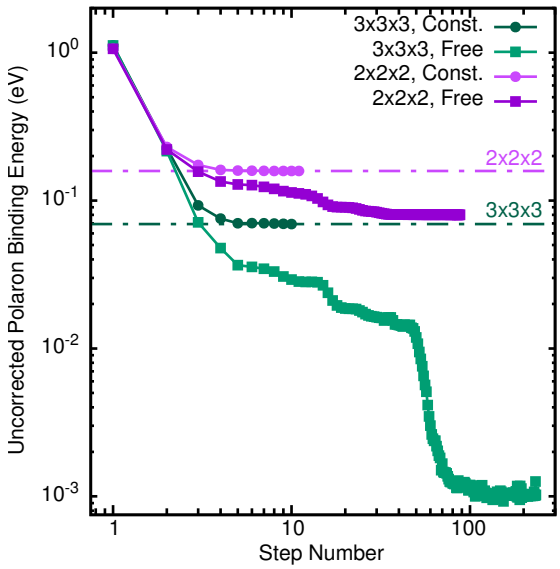

FIG. 6. The convergence of the free (squares) and constrained (circles) relaxation of a polaronic distortion in a 2x2x2 (purple) and 3x3x3 (green) supercell of rock-salt MgO. The zero of energy scale on is set to 1 meV below the energy of the fully relaxed structure. The horizontal dashed lines correspond to the final energy of constrained relaxation.

symmetry-reduced space. After explaining the algorithm, we test it on 340 different materials across a broad range of material classes. In all cases the new method was able to strictly preserve the symmetry of the materials, and on average reduced the number of steps needed to converge a material by 50%. We also demonstrated how the constraints can be used to relax to metastable phases, and relax structures with local symmetry braking with known distortion patterns.

This new method will have a profound impact on computational materials discovery. Not only does the decreased cost of relaxing a material increase the velocity of high-throughput search, but it also allows for those searches to explore metastable and dynamically stabilized structures. The method also has the promise to improve the efficiency of supercell calculations and study only the physically relevant structures. Finally by monitoring the difference between the full forces and symmeterized forces new stable phases can potentially be discovered from metastable or unstable polymorphs. Although we showed that the proposed algorithm is applicable to accelerate and improve standard solid-state physics calculations, its flexibility allows it to be applied to a much wider range of problems, e.g., transition-state searches. Similarly, it is easily generizable to other form of coordinates and straightforwardly implementable in any electronic-structure theory code.

V. ACKNOWLEDGEMENTS

TARP would like to acknowledge Florian Knoop for valuable discussions. This project was supported by TEC1p (the European Research Council (ERC) Horizon 2020 research and innovation programme, grant agreement No 740233), BigMax (the Max Planck Society's Research Network on Big-Data-Driven Materials-Science), and the NOMAD pillar of the FAIR-DI e.V. association. SC and DH acknowledges U.S. DOD-ONR (Grants No. N00014-17-1-2090). D.H. acknowledges support from the U.S. DOD through the National Defense Science and Engineering Graduate (NDSEG) Fellowship Program. We thank the Max Planck Computing and Data Facility for computational resources. The Authors declare no Competing Financial or Non-Financial Interests

VI. AUTHOR INFORMATION

A. Author Contributions

MOL and TARP contributed equally on this work by implementing and bench-marking the discussed relaxation scheme. DH worked to incorporate the constraints into AFLOW. SC, MS, and CC directed the project. All authors analysed the data and wrote the manuscript.

B. Competing Interests

The Authors declare no Competing Financial or Non-Financial Interests"

[1] P K Panda. Review: Environmental friendly lead-free piezoelectric materials. *Journal of Materials Science*, 44(19):5049–5062, 2009.

[2] Zhong Lin Wang. Progress in piezotronics and piezo-phototronics. *Advanced Materials*, 24(34):4632–4646, sep 2012.

[3] Kang Min Ok. Toward the Rational Design of Novel Noncentrosymmetric Materials: Factors Influencing the Framework Structures. *Accounts of Chemical Research*, 49(12):2774–2785, 2016.

[4] Thanh D. Nguyen, Sheng Mao, Yao Wen Yeh, Prashant K. Purohit, and Michael C. McAlpine. Nanoscale flexoelectricity. *Advanced Materials*, 25(7):946–974, feb 2013.

[5] Carlos Moure and Octavio Peña. Recent advances in perovskites: Processing and properties. *Progress in Solid State Chemistry*, 43(4):123–148, dec 2015.

[6] L. I. Isaenko, A. P. Yelisseyev, S. I. Lobanov, P. G. Krinitsin, and M. S. Molokeev. Structure and optical properties of Li2Ga2GeS6 nonlinear crystal. *Optical Materials*, 47:413–419, sep 2015.

[7] Dragan Damjanovic. Ferroelectric, dielectric and piezoelectric properties of ferroelectric thin films and ceramics. *Rep. Prog. Phys*, 61:1267, 1998.

[8] Tian Hang, Wen Zhang, Heng Yun Ye, and Ren Gen Xiong. Metal-organic complex ferroelectrics. *Chemical Society Reviews*, 40(7):3577–3598, jun 2011.

[9] Enwei Sun and Wenwu Cao. Relaxor-based ferroelectric single crystals: Growth, domain engineering, characterization and applications. *Progress in Materials Science*, 65:124–210, aug 2014.

[10] Ping Ping Shi, Yuan Yuan Tang, Peng Fei Li, Wei Qiang Liao, Zhong Xia Wang, Qiong Ye, and Ren Gen Xiong. Symmetry breaking in molecular ferroelectrics. *Chemical Society Reviews*, 45(14):3811–3827, jul 2016.

[11] R. J. Cava, Huiwen Ji, M. K. Fuccillo, Q. D. Gibson, and Y. S. Hor. Crystal structure and chemistry of topological insulators. *Journal of Materials Chemistry C*, 1(19):3176–3189, apr 2013.

[12] Gregory A. Fiete. Topological insulators: Crystalline protection. *Nature Materials*, 11(12):1003–1004, dec 2012.

[13] Owen R Evans and Wenbin Lin. Crystal engineering of NLO materials based on metal-organic coordination networks. *Accounts of Chemical Research*, 35(7):511–522, 2002.

[14] Kui Wu and Shilie Pan. A review on structure-performance relationship toward the optimal design of infrared nonlinear optical materials with balanced performances. *Coordination Chemistry Reviews*, 377:191–208, dec 2018.

[15] Jialiang Xu, Xinyue Li, Jianbo Xiong, Chunqing Yuan, Sergey Semin, Theo Rasing, and Xian-He Bu. Halide Perovskites for Nonlinear Optics. *Advanced Materials*, page 1806736, mar 2019.

[16] Minh Quy Le and Danh Truong Nguyen. The role of defects in the tensile properties of silicene. *Applied Physics A: Materials Science and Processing*, 118(4):1437–1445, mar 2014.

[17] Thi X.T. Sayle, Beverley J Inkson, Ajay Karakoti, Amit Kumar, Marco Molinari, Günter Möbus, Stephen C Parker, Sudipta Seal, and Dean C Sayle. Mechanical properties of ceria nanorods and nanochains; The effect of dislocations, grain-boundaries and oriented attachment. *Nanoscale*, 3(4):1823–1837, 2011.

[18] Xiaoyang Pan, Min Quan Yang, Xianzhi Fu, Nan Zhang, and Yi Jun Xu. Defective TiO2 with oxygen vacancies: Synthesis, properties and photocatalytic applications. *Nanoscale*, 5(9):3601–3614, 2013.

[19] Feng Wang, Jian Lin, Tingbi Zhao, Dandan Hu, Tao Wu, and Yang Liu. Intrinsic "vacancy Point Defect" Induced Electrochemiluminescence from Coreless Supertetrahedral Chalcogenide Nanocluster. *Journal of the American Chemical Society*, 138(24):7718–7724, 2016.

[20] Tae Ho An, Young Soo Lim, Hyoung Seuk Choi, Won Seon Seo, Cheol Hee Park, Gwi Rang Kim, Chan Park, Chang Hoon Lee, and Ji Hoon Shim. Point defect-assisted doping mechanism and related thermoelectric transport properties in Pb-doped BiCuOTe. *Journal of Materials Chemistry A*, 2(46):19759–19764, 2014.

[21] H. Anno, K. Matsubara, Y. Notohara, T. Sakakibara, and H. Tashiro. Effects of doping on the transport properties of CoSb3. *Journal of Applied Physics*, 86(7):3780–3786, oct 1999.

[22] Satyaprasad P. Senanayak, Bingyan Yang, Tudor H. Thomas, Nadja Giesbrecht, Wenchao Huang, Eliot Gann, Bhaskaran Nair, Karl Goedel, Suchi Guha, Xavier Moya, Christopher R. McNeill, Pablo Docampo, Aditya Sadhanala, Richard H. Friend, and Henning Sirringhaus. Understanding charge transport in lead iodide perovskite thin-film field-effect transistors. *Science Advances*, 3(1):e1601935, jan 2017.

[23] Vitaly S Proshchenko, Pratik P Dholabhai, Tyler C Sterling, and Sanghamitra Neogi. Heat and charge transport in bulk semiconductors with interstitial defects. *Physical Review B*, 99(1), 2019.

[24] Eric S Toberer, Andrew F May, and G Jeffrey Snyder. Zintl chemistry for designing high efficiency thermoelectric materials. *Chemistry of Materials*, 22(3):624–634, 2010.

[25] Hanhui Xie, Heng Wang, Yanzhong Pei, Chenguang Fu, Xiaohua Liu, G. Jeffrey Snyder, Xinbing Zhao, and Tiejun Zhu. Beneficial Contribution of Alloy Disorder to Electron and Phonon Transport in Half-Heusler Thermoelectric Materials. *Advanced Functional Materials*, 23(41):5123–5130, nov 2013.

[26] Jürgen Hafner. Ab-initio simulations of materials using VASP: Density-functional theory and beyond. *Journal of Computational Chemistry*, 29(13):2044–2078, oct 2008.

[27] Leeor Kronik, Adi Makmal, Murilo L. Tiago, M. M.G. Alemany, Manish Jain, Xiangyang Huang, Yousef Saad, and James R. Chelikowsky. PARSEC - The pseudopotential algorithm for real-space electronic structure calculations: Recent advances and novel applications to nano-structures. *Physica Status Solidi (B) Basic Research*, 243(5):1063–1079, apr 2006.

[28] R (Roger) Fletcher. *Practical methods of optimization*. Wiley, 1987.

[29] Jorge Nocedal and Stephen J Wright. *Numerical Optimization*. Springer, New York, NY, USA, second edition, 2006.

[30] Christoph Freysoldt. On-the-fly parameterization of internal coordinate force constants for quasi-Newton geometry optimization in atomistic calculations. *Computational Materials Science*, 133:71–81, jun 2017.

[31] Chiara Panosetti, Konstantin Krautgasser, Dennis Palagin, Karsten Reuter, and Reinhard J Maurer. Global Materials Structure Search with Chemically Motivated Coordinates. *Nano Letters*, 15(12):8044–8048, 2015.

[32] Volker Blum, Ralf Gehrke, Felix Hanke, Paula Havu, Ville Havu, Xinguo Ren, Karsten Reuter, and Matthias Scheffler. Ab initio molecular simulations with numeric atom-centered orbitals. *Computer Physics Communications*, 180(11):2175–2196, 2009.

[33] Franz Knuth, Christian Carbogno, Viktor Atalla, Volker Blum, and Matthias Scheffler. All-electron formalism for total energy strain derivatives and stress tensor components for numeric atom-centered orbitals. *Computer Physics Communications*, 190:33–50, may 2015.

[34] M H Bocanegra-Bernal and S Díaz de la Torre. Phase transitions in zirconium dioxide and related materials for high performance engineering ceramics. *Journal of Materials Science*, 37(23):4947–4971, 2002.

[35] David Hicks, Corey Oses, Eric Gossett, Geena Gomez, Richard H. Taylor, Cormac Toher, Michael J. Mehl, Ohad Levy, and Stefano Curtarolo. AFLOW-SYM: Platform for the complete, automatic and self-consistent symmetry analysis of crystals. *Acta Crystallographica Section A Foundations and Advances*, 74(3):184–203, may 2018.

[36] Michael J. Mehl, David Hicks, Cormac Toher, Ohad Levy, Robert M. Hanson, Gus Hart, and Stefano Curtarolo. The AFLOW Library of Crystallographic Prototypes: Part 1. *Computational Materials Science*, 136:S1–S828, aug 2017.

[37] David Hicks, Michael J. Mehl, Eric Gossett, Cormac Toher, Ohad Levy, Robert M. Hanson, Gus Hart, and Stefano Curtarolo. The AFLOW Library of Crystallographic Prototypes: Part 2. *Computational Materials Science*, 161:S1–S1011, apr 2019.

[38] Akifumi Matsumoto, Yukinori Koyama, and Isao Tanaka. Structures and energetics of Bi 2 O 3 polymorphs in a defective fluorite family derived by systematic first-principles lattice dynamics calculations. *Physical Review B*, 81(9):94117, mar 2010.

[39] Michel Drache, Pascal Roussel, and Jean-Pierre Wignacourt. Structures and Oxide Mobility in Bi-Ln-O Materials: Heritage of Bi_2O_3. *Chemical Reviews*, 107(1):80–96, 2007.

[40] Paolo Giannozzi, Stefano Baroni, Nicola Bonini, Matteo Calandra, Roberto Car, Carlo Cavazzoni, Davide Ceresoli, Guido L Chiarotti, Matteo Cococcioni, Ismaila Dabo, Andrea Dal Corso, Stefano de Gironcoli, Stefano Fabris, Guido Fratesi, Ralph Gebauer, Uwe Gerstmann, Christos Gougoussis, Anton Kokalj, Michele Lazzeri, Layla Martin-Samos, Nicola Marzari, Francesco Mauri, Riccardo Mazzarello, Stefano Paolini, Alfredo Pasquarello, Lorenzo Paulatto, Carlo Sbraccia, Sandro Scandolo, Gabriele Sclauzero, Ari P Seitsonen, Alexander Smogunov, Paolo Umari, and Renata M Wentzcovitch. QUANTUM ESPRESSO: a modular and open-source software project for quantum simulations of materials. *Journal of Physics: Condensed Matter*, 21(39):395502, sep 2009.

[41] X Gonze, J.-M. Beuken, R Caracas, F Detraux, M Fuchs, G.-M. Rignanese, L Sindic, M Verstraete, G Zerah, F Jollet, M Torrent, A Roy, M Mikami, Ph. Ghosez, J.-Y. Raty, and D C Allan. First-principles computation of material properties: the ABINIT software project. *Computational Materials Science*, 25(3):478–492, nov 2002.

[42] K Doll. Analytical stress tensor and pressure calculations with the CRYSTAL code. *Molecular Physics*, 108(3-4):223–227, 2010.

[43] C Radhakrishna Rao and Sujit Kumar Mitra. Generalized inverse of a matrix and its applications. In *Proceedings of the Sixth Berkeley Symposium on Mathematical Statistics and Probability, Volume 1: Theory of Statistics*, pages 601–620, Berkeley, Calif., 1972. University of California Press.

[44] Maja-Olivia Lenz, Thomas A.R. Purcell, David Hicks, Stefano Curtarolo, Matthias Scheffler, and Christian Carbogno. Constrained Geometry Relaxations: Dataset, 2019.

[45] Stefano Curtarolo, Wahyu Setyawan, Shidong Wang, Junkai Xue, Kesong Yang, Richard H. Taylor, Lance J. Nelson, Gus L.W. Hart, Stefano Sanvito, Marco Buongiorno-Nardelli, Natalio Mingo, and Ohad Levy. AFLOWLIB.ORG: A distributed materials properties repository from high-throughput ab initio calculations. *Computational Materials Science*, 58:227–235, jun 2012.

[46] Anubhav Jain, Shyue Ping Ong, Geoffroy Hautier, Wei Chen, William Davidson Richards, Stephen Dacek, Shreyas Cholia, Dan Gunter, David Skinner, Gerbrand Ceder, and Kristin A. Persson. Commentary: The materials project: A materials genome approach to accelerating materials innovation. *APL Materials*, 1(1):011002, jul 2013.

[47] Ask Hjorth Larsen, Jens JØrgen Mortensen, Jakob Blomqvist, Ivano E Castelli, Rune Christensen, Marcin Dułak, Jesper Friis, Michael N Groves, Bjørk Hammer, Cory Hargus, Eric D Hermes, Paul C Jennings, Peter Bjerre Jensen, James Kermode, John R Kitchin, Esben Leonhard Kolsbjerg, Joseph Kubal, Kristen Kaasbjerg, Steen Lysgaard, Jón Bergmann Maronsson, Tristan Maxson, Thomas Olsen, Lars Pastewka, Andrew Peterson, Carsten Rostgaard, Jakob SchiØtz, Ole Schütt, Mikkel Strange, Kristian S Thygesen, Tejs Vegge, Lasse Vilhelmsen, Michael Walter, Zhenhua Zeng, and Karsten W Jacobsen. The atomic simulation environment - A Python library for working with atoms. *Journal of Physics Condensed Matter*, 29(27):273002, jul 2017.

[48] David Hicks, Cormac Toher, Denise Ford, Frisco Rose, Carlo De Santo, Ohad Levy, Michael J. Mehl, and Stefano Curtarolo. AFLOW-XTAL-MATCH: Automated method for quantifying the structural similarity of materials and identifying unique crystal prototypes. *in preperation*, 2019.

[49] H Burzlaff and Y Malinovsky. A Procedure for the Clasification of Non-Organic Crystal Structures. I. Theoretical Background. *Acta Crystallographica Section A Foundations of Crystallography*,

53(2):217–224, mar 1997.

[50] Atsushi Togo and Isao Tanaka. *spglib*: a software library for crystal symmetry search. aug 2018.

[51] A Togo and I Tanaka. First principles phonon calculations in materials science. *Scr. Mater.*, 108:1–5, nov 2015.

[52] Renier Arabolla Rodríguez, Eduardo L. Pérez-Cappe, Yodalgis Mosqueda Laffita, Armando Chávez Ardanza, Jaime Santoyo Salazar, Manuel Ávila Santos, Miguel A. Aguilar Frutis, Nelcy Della Santina Mohalem, and Oswaldo Luiz Alves. Structural defects in LiMn2O4 induced by gamma radiation and its influence on the Jahn-Teller effect. *Solid State Ionics*, 324:77–86, oct 2018.

[53] Joseph C.A. Prentice, Bartomeu Monserrat, and R J Needs. First-principles study of the dynamic Jahn-Teller distortion of the neutral vacancy in diamond. *Physical Review B*, 95(1):14108, 2017.

[54] Robert Evarestov, Evgeny Blokhin, Denis Gryaznov, Eugene A Kotomin, Rotraut Merkle, and Joachim Maier. Jahn-Teller effect in the phonon properties of defective SrTiO 3 from first principles. *Physical Review B - Condensed Matter and Materials Physics*, 85(17):174303, 2012.

[55] Sebastian Kokott, Sergey V Levchenko, Patrick Rinke, and Matthias Scheffler. First-principles supercell calculations of small polarons with proper account for long-range polarization effects. *New Journal of Physics*, 20(3):033023, mar 2018.